Rapid Communications

Electronic band structure of (111) $SrRuO_3$ thin films: An angle-resolved photoemission spectroscopy study

Hanyoung Ryu,[1,2] Yukiaki Ishida,[1,3] Bongju Kim,[1,2] Jeong Rae Kim,[1,2] Woo Jin Kim,[1,2] Yoshimitsu Kohama,[3] Shusaku Imajo,[3] Zhuo Yang,[3] Wonshik Kyung,[1,2] Sungsoo Hahn,[1,2] Byungmin Sohn,[1,2] Inkyung Song,[1] Minsoo Kim,[1,2] Soonsang Huh,[1,2] Jongkeun Jung,[1,2] Donghan Kim,[1,2] Tae Won Noh,[1,2,*] Saikat Das,[1,2,†] and Changyoung Kim[1,2,‡]

[1]*Center for Correlated Electron Systems, Institute for Basic Science (IBS), Seoul 08826, Republic of Korea*

[2]*Department of Physics and Astronomy, Seoul National University (SNU), Seoul 08826, Republic of Korea*

[3]*Institute of Solid State Physics, The University of Tokyo, Kashiwa, Chiba 277-8581, Japan*

(Received 10 February 2020; revised 1 June 2020; accepted 15 June 2020; published 2 July 2020)

We studied the electronic band structure of pulsed laser deposition (PLD) grown (111)-oriented $SrRuO_3$ thin films using *in situ* angle-resolved photoemission spectroscopy technique. We observed light bands with a renormalized quasiparticle effective mass of about $0.8m_e$. The electron-phonon coupling underlying this mass renormalization yields a characteristic "kink" in the band dispersion. The self-energy analysis using the Einstein model suggests five optical phonon modes covering an energy range of 44–90 meV contribute to the coupling. In addition, we show that the quasiparticle spectral intensity at the Fermi level is considerably suppressed, and two prominent peaks appear in the valance band spectrum at binding energies of 0.8 and 1.4 eV, respectively. We discuss the possible implications of these observations. Overall, our work demonstrates that high-quality thin films of oxides with large spin-orbit coupling can be grown along the polar (111) orientation by the PLD technique, enabling *in situ* electronic band structure study. This could allow for characterizing the thickness-dependent evolution of band structure of (111) heterostructures—a prerequisite for exploring possible topological quantum states in the bilayer limit.

DOI: 10.1103/PhysRevB.102.041102

Perovskite transition metal oxides (TMOs) encompass a wide variety of properties such as high-temperature superconductivity, magnetism, ferroelectricity, metal-insulator transition, colossal magnetoresistance, and multiferroicity [1,2]. The plethora of physical properties in these materials originate from the subtle interplay among the charge, lattice, spin, and orbital degrees of freedom. Tweaking this interplay via epitaxy or heterointerfacing, furthermore, allows manipulating these properties and even designing novel phenomena or functionalities, which are unattainable by the bulk solid-state synthesis route. Examples include strain-induced enhancement of ferroelectricity and superconductivity [3,4], high-mobility conducting interface [5,6], interface ferromagnetism, and polar skyrmions [7,8]. While the majority of these works have been carried out using heterostructures that are grown along the crystallographic [001] direction, their (111)-oriented counterparts are gaining considerable attention recently [9–12].

Perhaps the biggest motivation to study (111)-oriented TMO heterostructures stems from the prediction of stabilizing novel topological phases in the bilayer limit [10,11]. Specific to this orientation, the trigonal crystal-field symmetry, together with a sizable spin-orbit coupling, is argued to open topologically protected energy gaps in an otherwise topologically trivial band structure. The strong electronic correlation that is inherent to the TMOs is further expected to enrich their topological properties. An essential step in this direction is first to comprehensively understand the band structure of thicker (111) TMO films, and subsequent characterization with thickness scaling. Thus, *in situ* angle-resolved photoemission spectroscopy (ARPES) studies could be highly beneficial, which, however, requires overcoming difficulties involved growing high-quality thin films on the polar (111) surfaces. In addition, the requirement of strong spin-orbit coupling (SOC) strength further narrows the choice of materials to the TMOs that contain heavier elements. Accordingly, to our best knowledge, ARPES studies on (111) thin films are limited to the 3*d* nickelates [13,14], where the SOC strength is expected to be weak. It is, therefore, instructive also exploring TMOs with larger SOC.

In this regard, $SrRuO_3$ (SRO), a 4*d* TMO, is of particular interest since both the SOC strength (0.1–0.15 eV) and electronic correlation are rather sizable [15,16]. In the bulk, SRO is an itinerant ferromagnet (below 165 K) and exhibits a Fermi-liquid behavior below 40 K [17]. Thin films of SRO that are grown along the [001] direction have been extensively studied as a model system in the context of anomalous Hall effect originating from the magnetic monopole in the momentum space [18,19]. Recently, it has gained renewed interest due to the observation of the topological Hall effect [7]. In addition, they are commonly used as metallic

*twnoh@snu.ac.kr

†Present address: Research Center for Magnetic and Spintronic Materials, National Institute for Materials Science, 1-2-1 Sengen, Tsukuba 305-0047, Japan; DAS.Saikat@nims.go.jp

‡changyoung@snu.ac.kr

electrodes, thanks to the feasibility of growing atomically smooth films with high crystalline quality. The electronic band structure of (001) SRO films is relatively well understood both on the theoretical [15,20–22] and the experimental fronts [17,23–26].

In contrast, the (111)-oriented SRO films have received moderate attention. Notably, (111) SRO thin films have been shown to exhibit anomalously enhanced magnetism (compared to the bulk), and conductivity compared to (001) SRO thin films [27–29]. It is also proposed that (111) SRO heterostructures could support half-metallic ground state at room temperature, and upon electron doping, a quantum anomalous Hall state could arise in the bilayer limit [30]. Both of these properties are highly relevant for spintronic applications. Despite these intriguing electromagnetic properties, the electronic band structure of (111) SRO films has not been studied experimentally [30].

In this Rapid Communication, we study the electronic band structure of (111) SRO thin film by means of an *in situ* APRES technique. We find the existence of a light band with a characteristic renormalized quasiparticle effective mass of $0.8m_e$. Based on the Einstein modeling of self-energy, we show that this mass renormalization can be attributed to the interaction between electrons and multiple phonon modes. Both the renormalized effective mass value, and the nature of the electron-phonon mode coupling differs from previously reported (001) SRO films, thereby highlighting the unique electronic property of (111) SRO film.

SRO thin films were grown on the B-site terminated (111)-oriented $SrTiO_3$ (STO) substrates [31] using the pulsed laser deposition technique (KrF laser, $\lambda = 248$ nm). During the growth, the substrate temperature and the background oxygen partial pressure were set to 680 °C and 100 mTorr, respectively. Meanwhile, the laser fluence and repetition rate were fixed to 1.1 J/cm^2 and 1 Hz, respectively. The growth dynamics were monitored by the reflection high-energy electron diffraction (RHEED) technique. After growth, samples were cooled down to room temperature, and the oxygen flow was stopped for achieving a high vacuum, $\sim 5 \times 10^{-9}$ Torr. After growth, the samples were transferred to the preparation chamber and postannealed in 1×10^{-9} Torr oxygen partial pressure at 510 °C for 30 min to achieve a clean surface. Subsequently, the films were transferred *in situ* to the ARPES chamber, which is equipped with a VG Scienta DA30 analyzer and ultraviolet light source and monochromator from Fermi instrument. During the ARPES measurement, the base pressure in the chamber was better than 8×10^{-11} Torr, and the sample temperature was 10 K. For the ARPES measurement, we employed He I (21.22 eV) light. X-ray photoemission spectroscopy (XPS) measurement was performed using an Al $K\alpha$ photon (1486.6 eV) at room temperature in the XPS analyzer chamber equipped with SPECS XR50 x-ray photon source (Fig. S1 in the Supplemental Material [32]). After the ARPES and XPS measurements, the samples were characterized by low-energy electron diffraction (LEED). Electrical transport measurement was performed by ultrasonically bonding gold wires onto the film in four-terminal configuration and using a Quantum Design physical property measurement system. The surface morphology was probed using an Asylum Cypher atomic force probe microscope (AFM).

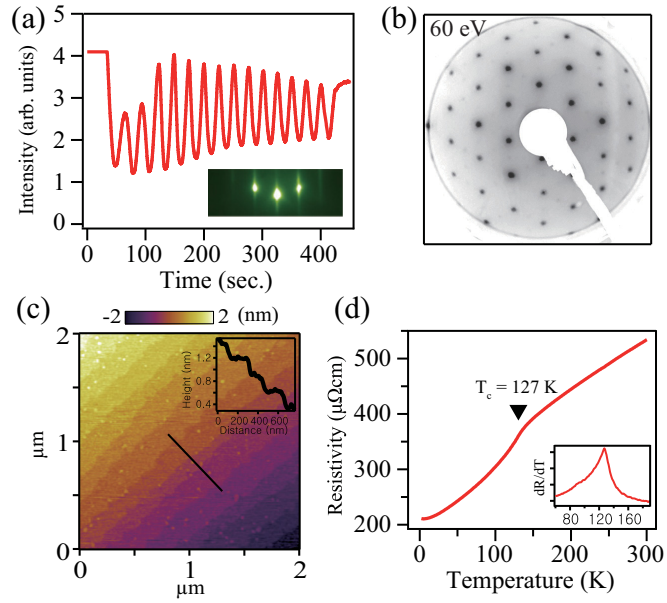

FIG. 1. (a) RHEED image taken along the [1$\bar{1}$0] azimuth. (b) LEED image of 15 u.c. SRO film, taken at an electron kinetic energy of 60 eV. (c) AFM image showing the step-terrace structure, and the inset shows the height profile along the black solid line. (d) Temperature-dependent resistivity of 15 u.c. (111) SRO, and the inset shows the derivative plot highlighting the onset of ferromagnetism around 127 K.

Figure 1(a) displays the characteristic RHEED intensity profile of the specular [00] Bragg reflex [inset of Fig. 1(a)] during SRO thin film growth. The specular RHEED intensity exhibits clear oscillations, reflecting the layer-by-layer growth of SRO film. The RHEED intensity oscillations enable us to precisely control the film thickness, which we varied between 7 and 30 unit cells (u.c.). As a representative figure, here, we have shown the RHEED intensity profile and pattern taken during and after the growth of a 15 u.c.-thick SRO film. As shown in the inset of Fig. 1(a), the RHEED pattern of the SRO film consists of sharp diffraction spots forming a Laue circle, which suggests coherent growth of crystalline domains with long-range ordering. This conjecture is further supported by the observation of a sharp LEED pattern [Fig. 1(b)], which following the sixfold symmetry of the (111) surface forms hexagonal motifs. In addition to intense principal spots, relatively weaker noninteger peaks are also discernible in the LEED image, which suggests the presence of surface reconstruction. AFM characterization further reveals that the film surface is atomically flat [Fig. 1(c)] and consists of a well-defined step-terrace structure with a nominal step height of 0.23 nm that amounts to the one-unit cell of SRO along the [111] direction. Transport measurement shows a metallic behavior [Fig. 1(d)] down to 2 K, along with a "kink" at 127 K that is characteristic of the onset of ferromagnetic phase transition. The residual resistivity $\sim 200\ \mu\Omega$ cm (at 2 K) compares well to the values reported for SRO (001) films of similar thickness [33]. Overall, the structural and electrical characterization demonstrates that high-quality SRO films can be grown on the (111) STO substrate.

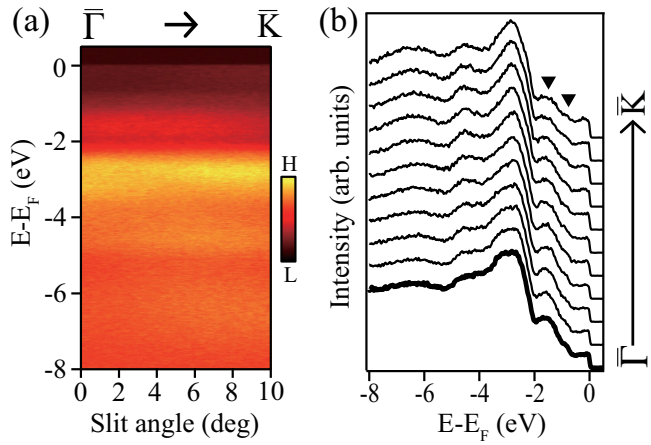

FIG. 2. (a) ARPES data over a wide energy window along the $\bar{\Gamma}$-$\bar{K}$ direction. (b) Corresponding angle-dependent EDC curves. Two triangles indicate the −1.4 and −0.8 eV peaks.

Next, to probe the electronic band structure of (111) SRO films, we measured APRES on SRO films with varying thicknessesof 7, 15, 30, and 50 u.c. While the thinnest film turns out to be insulating, ARPES measurements on the other three samples reveal a metallic nature with a sharp Fermi cutoff [34] [Fig. S2(a) in the Supplemental Material [32]]. Furthermore, the 15 u.c.-thick SRO film exhibits relatively sharper bands and clearer Fermi surface than the thicker samples. In the main text, we, therefore limit our discussion to the ARPES measurement performed on the 15 u.c.-thick SRO film. Figures 2(a) and 2(b) show the ARPES intensity plot along the high-symmetry $\bar{\Gamma}$-$\bar{K}$ direction of the Brillouin zone (BZ) [Fig. 3(a)] and the corresponding angle-dependent energy distribution curves (EDCs), respectively. The valance band spectra show weak dispersion along this high-symmetry direction. Nonetheless, the characteristic features associated with the O 2p nonbonding and bonding states between −3 and −7 eV [17,22] are discernible (Fig. S3 in the Supplemental Material [32]). Meanwhile, between −2 eV and the Fermi level, the EDC displays two unconventional peaks centered around −1.4 and −0.8 eV (marked by the triangles), alongside a considerably suppressed quasiparticle (QP) peak at the Fermi level. We found these features are common to all (111) SRO films, irrespective of their thicknesses (Fig. S2 in the Supplemental Material [32]).

To comprehend the origin of the suppressed QP intensity and the −1.4 eV peak, we compared the spectral weight of this peak for films with thickness ranging from 15 to 50 u.c. and found it to be thickness independent [Fig. (S2) in the Supplemental Material [32]]. The residual resistance ratio (RRR), obtained from the transport measurements, however, increases with increasing thickness. Assuming that the RRR value inversely correlates to the Ru vacancy concentration in the SRO film, we therefore argue that excessive Ru deficiency [17,24] cannot account for the −1.4 eV peak. Additionally, we studied an SRO film that was identically grown on the (001) STO substrate. The RRR value of this film (∼4) is slightly larger than the 15 u.c.-thick (111) film (∼2.5), but the Curie temperature (∼127 K) is identical. The valance band spectrum of this (001) SRO film exhibits a sharp QP peak, and is void of any additional peaks down to 2 eV from the Fermi level (Fig. S3 in the Supplemental Material [32]), which further supports our conjecture. Next, we consider disorders and enhanced electronic correlation, which can transfer spectral weight from the Fermi level to the so-called in-gap states and lower Hubbard band, respectively, yielding an incoherent

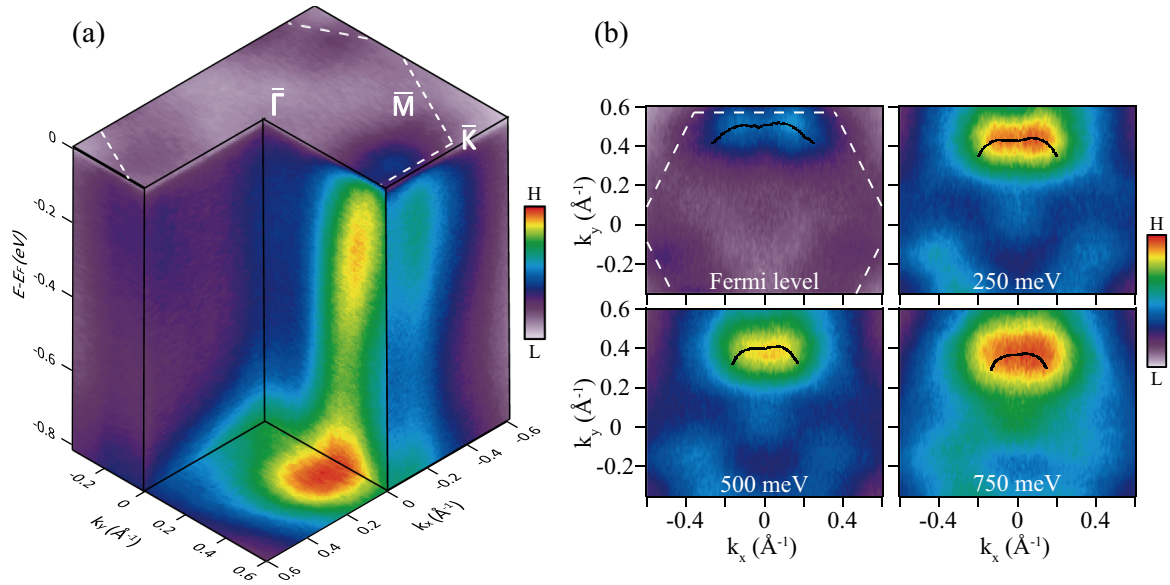

FIG. 3. (a) Three-dimensional energy versus momentum dispersion of the 15 u.c. SRO film. The dashed white line indicates the surface projected BZ. (b) Isoenergy surfaces at energies 0 (Fermi level), −250, −500, and −750 meV, respectively. These isoenergy surfaces are obtained by integrating over an energy window of +10 to −10 meV around the corresponding energies. The black dots are guides for the eyes, marking the coordinates of highest hotspot intensity that are obtained by profiling the isoenergy surfaces within the azimuthal angular range of +30° to −30°.

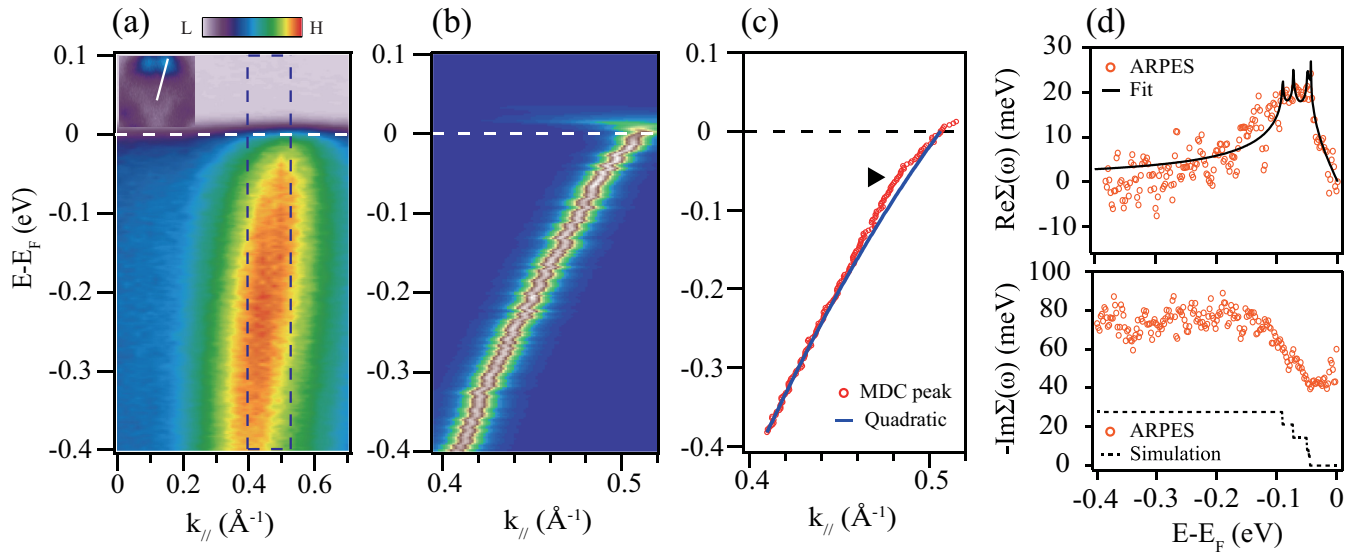

FIG. 4. (a) Energy versus momentum dispersion along the solid white line in the inset figure. (b) Two-dimensional curvature data zooming the marked rectangular region in (a). (c) The MDC dispersion (red circles) obtained by the Lorentzian fitting of MDC curves. The quadratic polynominal fit to the MDC is shown by the blue line. The black triangle indicates the "kink" in the dispersion. (d) The orange circles plot the real part, $\mathrm{Re}\Sigma(\omega)$ (upper panel), and the imaginary part, $\mathrm{Im}\Sigma(\omega)$ (lower panel), of the self-energy. The solid (dashed) black line marks the fit (simulation) of $\mathrm{Re}\Sigma(\omega)$ [$\mathrm{Im}\Sigma(\omega)$] using the Einstein model. The simulation is performed using parameters that are obtained by fitting $\mathrm{Re}\Sigma(\omega)$.

peak around −1.3 eV [25,35]. It is reasonable to expect that structural or compositional disorders could be present on the polar (111) surface as a means of compensating its polar charge. The single-peak structure of the O 1*s* XPS spectrum [36] [Fig. S1(a) in the Supplemental Material [32]], however, suggests that the contribution from the compositional disorders is minimal [35]. Structural disorders, namely, atomic reconstruction [evident in the LEED image Fig. 1(b)] and relaxation, therefore, naturally appear as the plausible driving mechanism. Understanding whether the structural disorders induce in-gap states or the lower Hubbard band requires further study, which is beyond the scope of this work.

Having examined the valance band of the (111) SRO film, we turn our attention to the fermiology. Figures 3(a) and 3(b) display the three-dimensional (3D) ARPES image and isoenergy surfaces covering binding energies down to −0.8 eV from the Fermi level. The Fermi surface consists of three hotspot pairs centered around the $\bar{M}$ points, forming six waterfall-like bands. The intensity of hotspots (or bands) exhibits azimuthal-angle dependence (Fig. S5 in the Supplemental Material [32]). This suggests the waterfall-like bands have a strong orbital character [37,38] that is possibly caused by the degeneracy lifting of the Ru t_{2g} states under the trigonal crystal field imposed by the (111) orientation [9]. Furthermore, the Fermi surface exhibits a threefold symmetry, which differs from the expected sixfold symmetry of the BZ [marked by the white dashed lines in Figs. 3(a) and 3(b)] projected on the (111) surface. This implies that for the given photon energy of 21.2 eV, we probe the three-dimensional bulk BZ away from the high-symmetry points (Γ or Z) along the k_z axis. Assuming a nominal inner potential value of about 14 eV [39], we estimate that we probe the bulk BZ around $k_z \sim 0.15\pi/c$, where $c = \sqrt{3}a_o$ with a_o (= 3.93 Å) being the pseudocubic lattice parameter of SRO.

With the increasing binding energy, the hotspot pairs shift towards the center of the BZ ($\bar{\Gamma}$). To better elaborate this shift, in Fig. 3(b) we mark the coordinates with the highest hotspot intensity by black dots. This binding-energy-dependent shift of the hotspot pairs reflects the dispersive nature of the waterfall-like bands, which is more prominent in the 3D ARPES image in Fig. 3(a). Tracking the band dispersion in Figs. 3(a) and 3(b), further reveals that the photoemission intensity nonmonotonically varies with the binding energy. First, it increases from the Fermi level to about −0.25 eV, followed by a dip through −0.5 eV before peaking at −0.8 eV. At binding energies higher than −0.8 eV, we could not observe a clear band dispersion due to overlap with the signal from the nondispersive −1.4 eV feature. From these observations, we conclude that the high photoemission intensity at −0.8 eV can be attributed to the bottom of the bands, which leads to the −0.8 eV peak in the valance band spectra [Fig. 2(b)]. In addition to the waterfall-like bands, we also observed a relatively weaker feature at the $\bar{\Gamma}$ point that vertically disperses down to −0.8 eV (Fig. S4 in the Supplemental Material [32]). At present, however, we do not understand the origin and implications of this vertically dispersive feature.

Next, to estimate the effective band mass and to gain insight into the many-body interactions, we further analyzed the waterfall-like band near the Fermi level. In Fig. 4(a) we show the band dispersion down to −0.4 eV, which is extracted along the cut marked by the white line in the inset figure. From the curvature plot [Fig. 4(b)] [40], which magnifies the dispersion between 0.4 and 0.52 Å^{-1} [dashed rectangle in Fig. 4(a)], we evaluated the corresponding Fermi wave vector to be about 0.51 Å^{-1}. Meanwhile, from the Lorentzian fitting of the

momentum distribution curves (MDCs) we obtained the MDC peak positions. The MDC peak dispersion is plotted using red circles in Fig. 4(c). With this information in hand, a quadratic polynomial fit to the high-binding energy part of the MDC peak dispersion [shown by the solid blue line in Fig. 4(c)], yields a bare band mass of about $m_b = 0.41 \pm 0.02 m_e$. In contrast, by fitting the dispersion within an energy range of ± 10 meV around the Fermi level, we obtained an effective quasiparticle $m^* = 0.76 \pm 0.04 m_e$. Therefore, the mass renormalization factor can be estimated to be about $m^*/m_b = 1.85 \pm 0.13$. Alternatively, from the ratio of the bare band velocity (v_b) to the quasiparticle velocity (v^*) we estimated the renormalization factor to be about 1.59 ± 0.13 (Fig. S6 in the Supplemental Material [32]). The comparable m^*/m_b and v_b/v^* values indicate the consistency of our approach. Interestingly, the renormalized quasiparticle mass (m^*) in (111) SRO is much lower than the values previously reported for (001) SRO films or layered Sr_2RuO_4, which nominally lie in the range $4–16 m_e$, and known to be strongly band dependent [17,41]. Recently, both light and heavy bands with m_b values of $1 m_e$ and $14 m_e$, respectively, have been found to coexist in $CaRuO_3$ [39]; these numbers are still larger than the band mass we obtained in this study. Although the extremely light band observed in (111) SRO films is surprising, it could be a natural consequence of probing a specific part of the BZ. This limitation perhaps also hinders observing other heavier bands.

The observation of quasiparticle mass renormalization suggests that the electrons couple with bosons, and the signature of this coupling can be found in the band dispersion. As evident in Fig. 4(c), the MDC dispersion deviates from the quadratic behavior between about 100 and 44 meV (marked by a triangle). For SRO, the observation of this so-called "kink" is attributed to the electron-phonon coupling [23]. To further support this assignment, in Fig. 4(d) we show the real part [$\mathrm{Re}\Sigma(\omega)$] and the imaginary part [$\mathrm{Im}\Sigma(\omega)$] of the self-energy that are calculated from the MDC. The real part of the self-energy [upper panel in Fig. 4(d)] exhibits a broad maximum covering an energy range similar to that of the kink. To quantitatively analyze the underlying electron-phonon coupling, we considered the Einstein model, which accounts for the coupling between electrons and optical phonons [42–48]. Assuming an effective electron-phonon coupling constant, $\lambda = 0.3$ and five optical phonon modes with energies $\hbar w_1 = 44.04$ meV, $\hbar w_2 = 46.4$ meV, $\hbar w_3 = 49.5$ meV, $\hbar w_4 = 72.7$ meV, and $\hbar w_5 = 90.44$ meV [49], we can fit $\mathrm{Re}\Sigma(\omega)$, as shown by the solid black line in the upper panel of Fig. 4(d). The imaginary part of the self-energy [lower panel of Fig. 4(d)], which is linked to the scattering rate of electrons, gradually increases from 44 meV and attains a plateau above 100 meV. Unlike $\mathrm{Re}\Sigma(\omega)$, the Einstein model, however, could not accurately describe the $\mathrm{Im}\Sigma(\omega)$. Although the simulation reproduces the increase in $\mathrm{Im}\Sigma(\omega)$ [dashed line in the lower panel of Fig. 4(d)], it could not account for a constant offset amounting to about ~45 meV. These discrepancies may be attributed to the additional contributions arising from the electron-defects scattering [43,50,51]. Nevertheless, the quantitative self-energy analysis demonstrates that the coupling between electrons and five optical phonon modes give rise to the kink in the band dispersion.

The relation between the electron-phonon coupling constant λ and the renormalization factor can be expressed as $m^*/m_b = v_b/v^* = (1 + \lambda)$. Based on the polynomial fitting of the MDC, therefore, λ should be in the range of 0.6–0.85, which is fairly comparable to the value ($= 0.9$) reported for the (001) SRO film [17]. Simulating the self-energy according to the Einstein model, with λ values of 0.6 and 0.85, however, leads to a large difference between the data and calculation (please see Fig. S7 and associated discussion in the Supplemental Material [32] for details). The discrepancy between λ values obtained using Einstein modeling of the self-energy and polynomial fitting of the MDC could arise due to the oversimplified assumption we made in the former approach; namely, the coupling strength to all phonon modes is identical. Therefore, we argue that $\lambda = 0.85$ should be treated as the upper bound of the electron-phonon coupling constant and might be envisaged as an effect of condensing five phonon modes' contributions into a single one.

In summary, we have demonstrated that high-quality SRO film can be grown along the polar (111) direction using the pulsed laser deposition technique. *In situ* ARPES study reveals the existence of light bands in the (111) SRO film. The effective mass analysis yields a renormalized quasiparticle effective mass of $\sim 0.8 m_e$, which is lowest among the ruthenates. The mass renormalization can be attributed to the coupling between electron and multiple phonon modes that yields characteristic kink in the band dispersion that spans an energy range between 100 and 44 meV. Also, we found that the quasiparticle spectral weight is suppressed at the Fermi level, and an incoherent peak appears at -1.4 eV, which we suggest possibly originates from the structural disorders that could be present on the polar (111) surface.

This work also leaves some open questions and scope for future studies. For example, we could not identify the orbital character of the observed bands, nor could we clarify the origin of the vertical feature at the Brillouin zone center. Synchrotron-based ARPES measurements with variable polarization and photon energies, complemented by theoretical calculations, could allow for comprehensively understanding the overall band structure, including the orbital character of the band and the vertical feature. Nevertheless, we hope that our work would further stimulate studies on (111) thin films of correlated oxides with strong spin-orbit coupling strength and eventually pave the way towards realizing novel topological quantum phases.

This work was supported by the Institute for Basic Science in Korea, Grants No. IBS-R009-G2 and No. IBS-R009-D1.

S.D. conceived and designed the research under the direction of T.W.N. S.D. grew and characterized samples assisted by J.R.K., S.H., B.S., and D.K. B.K., S.D., W.J.K., Y.K., S.I., and Z.Y. performed transport measurements. H.R., S.D., and B.K. studied the optimized sample cleaning condition. H.R. performed the ARPES and XPS measurements under the supervision of C.K. and with assistance from I.S., M.K., S.H., J.J., S.H., and W.K., H.R., and Y.I. analyzed the data. H.R., S.D., Y.I., and C.K. discussed and interpreted the results. H.R. and S.D. wrote the manuscript with input from all the authors.

[1] M. Imada, A. Fujimori, and Y. Tokura, Rev. Mod. Phys. **70**, 1039 (1998).

[2] R. Ramesh and N. A. Spaldin, Nat. Mater. **6**, 21 (2007).

[3] K. J. Choi, M. Biegalski, Y. L. Li, A. Sharan, J. Schubert, R. Uecker, P. Reiche, Y. B. Chen, X. Q. Pan, V. Gopalan, L.-Q. Chen, D. G. Schlom, and C. B. Eom, Science **306**, 1005 (2004).

[4] I. Bozovic, G. Logvenov, I. Belca, B. Narimbetov, and I. Sveklo, Phys. Rev. Lett. **89**, 107001 (2002).

[5] H. Lee, N. Campbell, J. Lee, T. J. Asel, T. R. Paudel, H. Zhou, J. W. Lee, B. Noesges, J. Seo, B. Park, L. J. Brillson, S. H. Oh, E. Y. Tsymbal, M. S. Rzchowski, and C. B. Eom, Nat. Mater. **17**, 231 (2018).

[6] A. Ohtomo and H. Y. Hwang, Nature (London) **427**, 423 (2004).

[7] J. Matsuno, N. Ogawa, K. Yasuda, F. Kagawa, W. Koshibae, N. Nagaosa, Y. Tokura, and M. Kawasaki, Sci. Adv. **2**, e1600304 (2016).

[8] K.-Y. Meng, A. S. Ahmed, M. Bacáni, A.-O. Mandru, X. Zhao, N. Bagués, B. D. Esser, J. Flores, D. W. McComb, H. J. Hug, and F. Yang, Nano Lett. **19**, 3169 (2019).

[9] S. Okamoto, W. Zhu, Y. Nomura, R. Arita, D. Xiao, and N. Nagaosa, Phys. Rev. B **89**, 195121 (2014).

[10] S. Okamoto and D. Xiao, J. Phys. Soc. Jpn. **87**, 041006 (2018).

[11] K.-Y. Yang, W. Zhu, D. Xiao, S. Okamoto, Z. Wang, and Y. Ran, Phys. Rev. B **84**, 201104(R) (2011).

[12] S. Middey, D. Meyers, D. Doennig, M. Kareev, X. Liu, Y. Cao, Z. Yang, J. Shi, L. Gu, P. J. Ryan, R. Pentcheva, J. W. Freeland, and J. Chakhalian, Phys. Rev. Lett. **116**, 056801 (2016).

[13] F. Y. Bruno, M. Gibert, S. McKeown Walker, O. E. Peil, A. de la Torre, S. Ricco, Z. Wang, S. Catalano, A. Tamai, F. Bisti, V. N. Strocov, J.-M. Triscone, and F. Baumberger, APL Mater. **5**, 016101 (2017).

[14] A. Arab, X. Liu, O. Köksal, W. Yang, R. U. Chandrasena, S. Middey, M. Kareev, S. Kumar, M.-A. Husanu, Z. Yang, L. Gu, V. N. Strocov, T.-L. Lee, J. Minár, R. Pentcheva, J. Chakhalian, and A. X. Gray, Nano Lett. **19**, 8311 (2019).

[15] J. M. Rondinelli, N. M. Caffrey, S. Sanvito, and N. A. Spaldin, Phys. Rev. B **78**, 155107 (2008).

[16] L. F. Mattheiss, Phys. Rev. B **13**, 2433 (1976).

[17] D. E. Shai, C. Adamo, D. W. Shen, C. M. Brooks, J. W. Harter, E. J. Monkman, B. Burganov, D. G. Schlom, and K. M. Shen, Phys. Rev. Lett. **110**, 087004 (2013).

[18] G. Koster, L. Klein, W. Siemons, G. Rijnders, J. S. Dodge, C.-B. Eom, D. H. A. Blank, and M. R. Beasley, Rev. Mod. Phys. **84**, 253 (2012).

[19] Z. Fang, N. Nagaosa, K. S. Takahashi, A. Asamitsu, R. Mathieu, T. Ogasawara, H. Yamada, M. Kawasaki, Y. Tokura, and K. Terakura, Science **302**, 92 (2003).

[20] M. Kim and B. I. Min, Phys. Rev. B **91**, 205116 (2015).

[21] E. Jakobi, S. Kanungo, S. Sarkar, S. Schmitt, and T. Saha-Dasgupta, Phys. Rev. B **83**, 041103(R) (2011).

[22] K. Fujioka, J. Okamoto, T. Mizokawa, A. Fujimori, I. Hase, M. Abbate, H. J. Lin, C. T. Chen, Y. Takeda, and M. Takano, Phys. Rev. B **56**, 6380 (1997).

[23] H. F. Yang, Z. T. Liu, C. C. Fan, Q. Yao, P. Xiang, K. L. Zhang, M. Y. Li, H. Li, J. S. Liu, D. W. Shen, and M. H. Jiang, Phys. Rev. B **93**, 121102(R) (2016).

[24] W. Siemons, G. Koster, A. Vailionis, H. Yamamoto, D. H. A. Blank, and M. R. Beasley, Phys. Rev. B **76**, 075126 (2007).

[25] H. F. Yang, C. C. Fan, Z. T. Liu, Q. Yao, M. Y. Li, J. S. Liu, M. H. Jiang, and D. W. Shen, Phys. Rev. B **94**, 115151 (2016).

[26] D. Toyota, I. Ohkubo, H. Kumigashira, and M. Oshima, Appl. Phys. Lett. **87**, 162508 (2005).

[27] A. Grutter, F. Wong, E. Arenholz, M. Liberati, A. Vailionis, and Y. Suzuki, Appl. Phys. Lett. **96**, 082509 (2010).

[28] B. Lee, O. Kwon, R. H. Shin, W. Jo, and C. U. Jung, Nanoscale Res. Lett. **9**, 8 (2014).

[29] X. K. Ning, Z. J. Wang, and Z. D. Zhang, J. Appl. Phys. **117**, 093907 (2015).

[30] L. Si, O. Janson, G. Li, Z. Zhong, Z. Liao, G. Koster, and K. Held, Phys. Rev. Lett. **119**, 026402 (2017).

[31] I. Hallsteinsen, M. Nord, T. Bolstad, P. Vullum, J. E. Boschker, P. Longo, R. Takahashi, R. Holmestad, M. Lippmaa, and T. Tybell, Cryst. Growth Des. **16**, 2357 (2016).

[32] See Supplemental Material at http://link.aps.org/supplemental/10.1103/PhysRevB.102.041102 for additional information on XPS, thickness-dependent, and orientation-dependent angle integrated spectra and RRR from various of SRO films, analysis of renormalized factor, Fermi surface measured with different azimuthal angle, and the Einstein model simulation with different parameters.

[33] J. Xia, W. Siemons, G. Koster, M. R. Beasley, and A. Kapitulnik, Phys. Rev. B **79**, 140407(R) (2009).

[34] A. Rastogi, M. Brahlek, J. M. Ok, Z. Liao, C. Sohn, S. Feldman, and H. N. Lee, APL Materials **7**, 091106 (2019).

[35] J. Kim, J. Chung, and S.-J. Oh, Phys. Rev. B **71**, 121406(R) (2005).

[36] Y. Ishida, R. Eguchi, M. Matsunami, K. Horiba, M. Taguchi, A. Chainani, Y. Senba, H. Ohashi, H. Ohta, and S. Shin, Phys. Rev. Lett. **100**, 056401 (2008).

[37] T. Sugimoto, D. Ootsuki, C. Morice, E. Artacho, S. S. Saxena, E. F. Schwier, M. Zheng, Y. Kojima, H. Iwasawa, K. Shimada, M. Arita, H. Namatame, M. Taniguchi, M. Takahashi, N. L. Saini, T. Asano, R. Higashinaka, T. D. Matsuda, Y. Aoki, and T. Mizokawa, Phys. Rev. B **92**, 041113(R) (2015).

[38] Y. Aiura, I. Hase, H. Bando, K. Yagi-Watanabe, K. Ozawa, T. Iwase, Y. Nishihara, O. Shiino, M. Oshima, M. Kubota, and K. Ono, Phys. Rev. Lett. **91**, 256404 (2003).

[39] Y. Liu, H. P. Nair, J. P. Ruf, D. G. Schlom, and K. M. Shen, Phys. Rev. B **98**, 041110(R) (2018).

[40] P. Zhang, P. Richard, T. Qian, Y.-M. Xu, X. Dai, and H. Ding, Rev. Sci. Instrum. **82**, 043712 (2011).

[41] A. Tamai, M. Zingl, E. Rozbicki, E. Cappelli, S. Riccò, A. de la Torre, S. McKeown Walker, F. Y. Bruno, P. D. C. King, W. Meevasana, M. Shi, M. Radović, N. C. Plumb, A. S. Gibbs, A. P. Mackenzie, C. Berthod, H. U. R. Strand, M. Kim, A. Georges, and F. Baumberger, Phys. Rev. X **9**, 021048 (2019).

[42] C. Kirkegaard, T. K. Kim, and Ph. Hofmann, New J. Phys. **7**, 99 (2005).

[43] P. Hofmann, I. Yu. Sklyadneva, E. D. L. Rienks, and E. V. Chulkov, New J. Phys. **11**, 125005 (2009).

[44] *Very High Resolution Photoelectron Spectroscopy*, edited by S. Hüfner (Springer, Berlin, 2007).

[45] S. R. Park, D. J. Song, C. S. Leem, C. Kim, C. Kim, B. J. Kim, and H. Eisaki, Phys. Rev. Lett. **101**, 117006 (2008).

[46] D. M. Tang, J. Li, and C.-D. Gong, Phys. Rev. B **67**, 235421 (2003).

[47] A. Tamai, W. Meevasana, P. D. C. King, C. W. Nicholson, A. de la Torre, E. Rozbicki, and F. Baumberger, Phys. Rev. B **87**, 075113 (2013).

[48] P. M. Echenique, R. Berndt, E. V. Chulkov, Th. Fauster, A. Goldmann, and U. Höfer, Surf. Sci. Rep. **52**, 219 (2004).

[49] B. C. Behera, P. Padhan, and W. Prellier, Phys. J. Magn. Magn. Mater. **388**, 22 (2015).

[50] M. A. López de la Torre, Z. Sefrioui, D. Arias, M. Varela, J. E. Villegas, C. Ballesteros, C. León, and J. Santamaría, Phys. Rev. B **63**, 052403 (2001).

[51] E. V. Chulkov, A. G. Borisov, J. P. Gauyacq, D. Sánchez-Portal, V. M. Silkin, V. P. Zhukov, and P. M. Echenique, Chem. Rev. **106**, 4160 (2006).